ACS OMEGA

http://pubs.acs.org/journal/acsodf

Article

# Simulation of Microscopic Seepage Characteristics of Interphase Mass Transfer in $CO_2$ Miscible Flooding under Multiphysics Field Coupling Conditions

Jing Li, Chuanzhi Cui,* Zhongwei Wu, Jiqing Yi, Ran Zong, Yihui Fu, and Xingyuan Han

Cite This: *ACS Omega* 2023, 8, 10062−10076

Read Online

ACCESS | Metrics & More | Article Recommendations

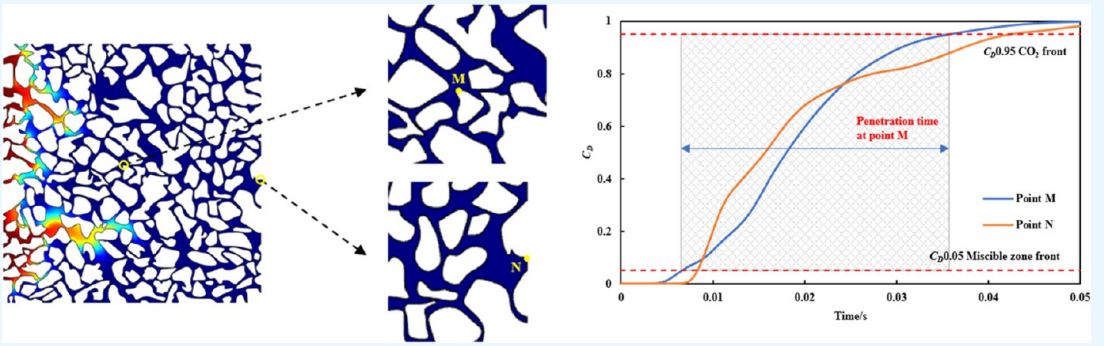


**ABSTRACT:** $CO_2$ miscible flooding in low permeability reservoirs is conducive to significantly improving oil recovery. At present, the microscopic displacement simulation of $CO_2$ miscible flooding is mainly reflected in the simulation of the seepage process, but the pressure control of the seepage process is lacking, and the simulation of the characterization of $CO_2$ concentration diffusion is less studied. In view of the above problems, a numerical model of $CO_2$ miscible flooding is established, and the microscopic seepage characteristics of interphase mass transfer in $CO_2$ miscible flooding are analyzed by multiphysics field coupling simulations at the two-dimensional pore scale. The injection velocity, contact angle, diffusion coefficient, and initial injection concentration are selected to analyze their effects on the microscopic seepage characteristics of $CO_2$ miscible flooding and the concentration distribution in the process of $CO_2$ diffusion. The research shows that after injection into the model, $CO_2$ preferentially diffuses into the large pore space and forms a miscible area with crude oil through interphase mass transfer, and the miscible area expands continuously and is pushed to the outlet by the high $CO_2$ concentration area. The increase in injection velocity will accelerate the seepage process of $CO_2$ miscible displacement, which will increase the sweep area at the same time. The increase in contact angle increases the seepage resistance of $CO_2$ and weakens the interphase mass transfer with crude oil, resulting in a gradual decrease in the final recovery efficiency. When the diffusion coefficient increases, the $CO_2$ concentration in the small pores and the parts that are difficult to reach at the model edge will gradually increase. The larger the initial injection concentration is, the larger the $CO_2$ concentration in the large pore and miscible areas in the sweep region at the same time. This study has guiding significance for the field to further understand the microscopic seepage characteristics of $CO_2$ miscible flooding under the effect of interphase mass transfer.

## 1. INTRODUCTION

$CO_2$ is an effective oil displacement agent in low permeability reservoirs.[1] Through multistage contact, miscible $CO_2$ flooding can form a miscible area. In the miscible area, the interfacial tension between $CO_2$ and crude oil disappears, the viscosity of crude oil is greatly reduced, and the mobility is enhanced, showing a good oil displacement effect.[2,3] However, when gas is found in the production well, $CO_2$ will form an ineffective cycle due to gas channeling. Understanding the seepage characteristics and concentration variation of $CO_2$ at the pore scale during miscible flooding is of great significance for the field to further comprehend the mechanism of miscible flooding and identify the timing of gas channeling.

At present, physical simulation[4−9] and numerical simulation methods[10,11] are mainly used in the research of $CO_2$ miscible flooding. In physical simulations, core displacement experiments[12−14] and nuclear magnetic resonance experiments[15,16] are mainly used to study the migration law of $CO_2$ under macroscopic conditions. Numerical simulation methods mainly

Received: November 17, 2022
Accepted: February 20, 2023
Published: March 9, 2023

focus on the establishment of convection−diffusion equations[17,18] and the simulation of macroscopic and microscopic seepage processes.[19,20] In terms of numerical simulation, Ju et al.[21] established a multicomponent nonisothermal $CO_2$ miscible displacement mathematical model and developed a numerical simulation program to predict the process of $CO_2$ miscible displacement. Afshari et al.[22] used pore-scale numerical simulation to study the flow and transport dynamics during miscible flooding with a reverse viscosity ratio in the heterogeneous round particle model and normalized the length−time curve of the miscible zone relative to the control parameters, such as the viscosity ratio, heterogeneity, medium length, and medium aspect ratio. Bhatti et al.[23] evaluated a miscible $CO_2$ flooding reservoir in Pakistan by applying improved screening criteria and numerical simulation. According to the results obtained, the southern reservoir (S3) is selected for detailed evaluation of $CO_2$ miscible flooding. Ma et al.[24] studied the flow behavior of $CO_2$ under the conditions of immiscible flooding and miscible flooding at the pore scale through numerical simulation. The study pointed out that compared with immiscible flooding, miscible flooding can increase the sweep area, and improving the injection velocity is beneficial to accelerate the oil displacement process. In summary, $CO_2$ dissolves in crude oil and extracts light components of crude oil to form a miscible area through mass transfer and diffusion during miscible flooding. The above research has reference significance for simulating the flow behavior of $CO_2$ miscible flooding, but there are few simulation studies on pressure control and $CO_2$ concentration diffusion characteristics in the process of $CO_2$ miscible flooding at the microscopic pore scale.

In view of the above research problems, this paper establishes a numerical model of $CO_2$ miscible flooding based on COMSOL Multiphysics simulation software and analyzes the microscopic seepage characteristics of $CO_2$ miscible flooding combined with a two-dimensional pore model. The injection velocity, contact angle, diffusion coefficient, and initial injection concentration are selected from the injection parameters, wall wettability, $CO_2$ diffusion ability, and other aspects to analyze their effects on the microscopic seepage characteristics of $CO_2$ miscible flooding and the concentration distribution in the process of $CO_2$ diffusion. This study has guiding significance for the field to further understand the microscopic seepage characteristics and concentration distribution characteristics of $CO_2$ miscible flooding under the effect of interphase mass transfer.

## 2. METHODS

**2.1. Establishment of a Numerical Model for $CO_2$ Miscible Flooding.** During miscible flooding, $CO_2$ mainly contacts crude oil in the form of convection−diffusion in the formation. After multistage contact, the interfacial tension between the gas phase and oil phase disappears, forming a miscible area. To simulate the microscopic seepage characteristics of $CO_2$ miscible flooding in porous media, the following assumptions need to be made: (1) Ignore the compressibility of the fluid within the porous medium and the porous medium itself. (2) The diffusion coefficient does not depend on the concentration of the fluid injected into the porous medium and ignores the molar diffusion phenomenon. (3) Without considering the chemical reactions between different substances inside the porous medium and the adsorption of the injected gas, it is assumed that the volume and shape of the porous medium do not change during the displacement process. (4) Ignore the change in contact angle. (5) $CO_2$ can be fully mixed with the oil, but the resulting volume change in oil expansion and oil extraction is negligible.[24] (6) $CO_2$ and crude oil are considered Newtonian fluids. (7) The diffusion coefficient does not change during displacement. (8) The classical Fick's law is applicable to diffusion in miscible areas.

*2.1.1. Laminar Flow Equations.* The mass conservation of an incompressible fluid is expressed by the continuity equation as follows

$$\nabla\cdot\mathbf{u} = 0 \tag{1}$$

where $\mathbf{u}$ is the fluid velocity, $m\cdot s^{-1}$.

Without considering gravity, the momentum balance of the fluid is characterized by the incompressible Navier−Stokes equation as follows[24]

$$\rho\frac{\partial\mathbf{u}}{\partial t} + \rho(\mathbf{u}\cdot\nabla)\mathbf{u} = \nabla\cdot\{-p\mathbf{I} + \mu[\nabla\mathbf{u} + (\nabla\mathbf{u})^T]\} + \mathbf{F}_{st} \tag{2}$$

where $\rho$ represents the fluid density, $kg\cdot m^{-3}$; $t$ equals the time, s; $p$ is the pressure, Pa; $\mathbf{I}$ represents the identity matrix; $\mu$ is the fluid viscosity, Pa·s; and $\mathbf{F}_{st}$ is the surface tension force between two phases, $Pa\cdot m^{-1}$, $\mathbf{F}_{st} = 0$ under the condition of $CO_2$ miscible flooding.

The formula of the wall boundary condition for no-slip is as follows

$$\mathbf{u} = 0 \tag{3}$$

The boundary condition formula of inlet velocity is as follows

$$\mathbf{u} = -U_0\mathbf{n} \tag{4}$$

where $U_0$ is the normal inflow velocity, $m\cdot s^{-1}$, and $\mathbf{n}$ is the normal vector.

The formula of the outlet pressure boundary condition is as follows

$$\{-p\mathbf{I} + \mu[\nabla\mathbf{u} + (\nabla\mathbf{u})^T]\}\mathbf{n} = -\hat{p}_0\mathbf{n} \tag{5}$$

where $\hat{p}_0$ is the outlet pressure, Pa.

*2.1.2. Phase-Field Equations.* Two phase components in two-phase flow are represented by the phase-field function $\phi$ and are considered pure components in $\phi = \pm 1$. When $\phi$ is between 1 and −1, it represents a two-phase interface. The $CO_2$ phase-field function is $\phi = 1$, and the oil phase-field function is $\phi = -1$. The convective Cahn−Hilliard equation can be written as[1]

$$\frac{\partial\phi}{\partial t} + \mathbf{u}\cdot\nabla\phi = \nabla\cdot\frac{\gamma\lambda}{\varepsilon^2}\nabla\psi \tag{6}$$

$$\psi = -\nabla\cdot\varepsilon^2\nabla\phi + (\phi^2 - 1)\phi \tag{7}$$

where the equations of $\gamma$ and $\lambda$ are as follows

$$\gamma = \chi\varepsilon^2, \qquad \lambda = \frac{3\sqrt{2}\,\varepsilon\sigma}{4}$$

where $\phi$ is the phase-field variable, dimensionless; $\gamma$ is the mobility, $m^3\cdot s\cdot kg^{-1}$; $\lambda$ is the mixing energy density, $N$; $\varepsilon$ is the interface thickness parameter, $m$; $\psi$ is referred to as the phase-field help variable; $\chi$ is the mobility adjustment parameter, $m\cdot s\cdot kg^{-1}$; and $\sigma$ is the surface tension coefficient, $N\cdot m^{-1}$.

In the phase-field interface, the diffuse interface representation makes it possible to compute the surface tension by



https://doi.org/10.1021/acsomega.2c07393
ACS Omega 2023, 8, 10062−10076

$$\mathbf{F}_{st} = G\nabla\phi \tag{8}$$

$$G = \lambda\left[-\nabla^2\phi + \frac{\phi(\phi^2-1)}{\varepsilon^2}\right] = \frac{\lambda}{\varepsilon^2}\psi \tag{9}$$

where $G$ is the chemical potential, J·m$^{-3}$.

At the phase-field interface, the volume fractions of the individual fluids are as follows

$$V_{f,1} = \frac{1-\phi}{2} \tag{10}$$

$$V_{f,2} = \frac{1+\phi}{2} \tag{11}$$

$$V_{f,1} + V_{f,2} = 1 \tag{12}$$

where $V_{f,1}$ is the volume fraction of the oil phase, dimensionless, and $V_{f,2}$ is the volume fraction of $CO_2$, dimensionless.

The wetted wall default boundary condition is imposed on the boundary. Mathematically, the boundary condition is as follows

$$\mathbf{n}\cdot\varepsilon^2\nabla\phi = \varepsilon^2\cos\theta|\nabla\phi| \tag{13}$$

$$\mathbf{n}\cdot\frac{\gamma\lambda}{\varepsilon^2}\nabla\psi = 0 \tag{14}$$

where $\theta$ is the contact angle, °. The contact angle is set as the angle between the solid−gas interface and the liquid−gas interface, that is, the angle is between $CO_2$ and rock.

The interface normal $\mathbf{n}$ is calculated as

$$\mathbf{n} = \frac{\nabla\phi}{|\nabla\phi|} \tag{15}$$

The multiphysics coupling feature defines the density and the viscosity of the mixture to vary smoothly over the interface by letting

$$\rho = \rho_{oil} + (\rho_{CO_2} - \rho_{oil})V_{f,2} \tag{16}$$

$$\mu = \mu_{oil} + (\mu_{CO_2} - \mu_{oil})V_{f,2} \tag{17}$$

The inlet boundary equation is as follows

$$\phi = 2V_f - 1 \tag{18}$$

where $V_f$ is the fluid volume fraction, dimensionless. The inlet value of the phase-field function is $\phi = 1$, that is, the injected fluid is $CO_2$.

*2.1.3. Transport of Diluted Species Equations.* The mass balance describing the mass transfer in pores is established through the physical field of transport of diluted species, in which diffusion and convection are considered. The equation is as follows

$$\frac{\partial c}{\partial t} + \nabla\cdot(-D\nabla c) + \mathbf{u}\cdot\nabla c = 0 \tag{19}$$

where $D$ denotes the diffusion coefficient, m$^2$·s$^{-1}$, and $c$ represents the $CO_2$ concentration in the pore space, mol·m$^{-3}$.

The no-flux boundary condition equation is as follows

$$-\mathbf{n}\cdot(-D\nabla c) = 0 \tag{20}$$

The inlet concentration boundary condition equation is as follows

$$c = c_0 \tag{21}$$

where $c_0$ represents the $CO_2$ injection concentration at the inlet, mol·m$^{-3}$.

The outflow boundary condition equation is as follows

$$\mathbf{n}\cdot D\nabla c = 0 \tag{22}$$

**2.2. Validation of the Numerical Model.** A case is used to verify the numerical model, as shown in Figure 1. This case

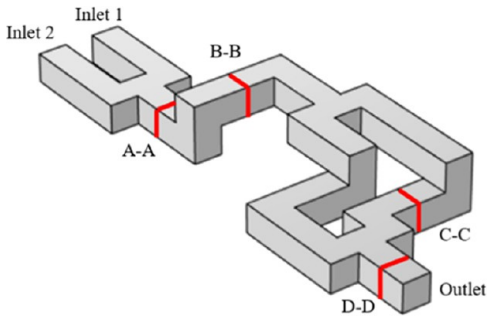


**Figure 1.** Model diagram.

simulates the fluid flow in a separation and recombination mixer, where a tracer fluid is introduced in the channel and mixed by multiple laminar flows. A very low diffusion coefficient is used to remove the diffusion effect from the model to study the numerical diffusion in the laminar flow interface. The results are compared with the experimental results of Glatzel et al.,[25] and they are very consistent in the laminar flow pattern and the total pressure drop of the mixer (Figures 2 and 3).

Table 1 shows that at a given flow rate, the numerical simulation result of the total pressure drop of the mixer is 1.630 Pa. The numerical simulation results are slightly lower than those obtained by Glatzel et al.[25] However, because the finite element method adds less artificial diffusion to the problem than the finite volume method, the expected value is low. Adding artificial diffusion to the flow problem will increase the effective viscosity of the fluid, so it is expected to artificially increase the pressure drop of the whole system. Therefore, the above numerical model is applicable to the simulation of interphase mass transfer in $CO_2$ miscible flooding.

**2.3. Establishment of a Two-Dimensional Model.** The core used for simulation has a permeability of 1.237 mD and a porosity of 12.61%. The casting thin section and scanning electron microscope data of the core were screened, and the obtained images were processed to obtain a two-dimensional pore model, as shown in Figure 4. The left side of the two-dimensional model is the inlet side, and the right side is the outlet side. The two-dimensional model diagram is imported into the geometry of COMSOL Multiphysics for simulation research.

**2.4. Material Parameters.** The minimum miscible pressure of $CO_2$ and crude oil (*n*-decane) for simulation at 343 K is 12.4 MPa. The density, viscosity, and diffusion coefficient between $CO_2$ and crude oil under simulation conditions are derived from the work of Ma et al.,[24] as shown in Table 2.

**2.5. Initial Parameter Setting.** The two-phase flow phase field includes the laminar flow physical field and the phase-field physical field. In the laminar flow physical field, the reference pressure level $p_{ref}$ is the default value of 1 atm, the reference


https://doi.org/10.1021/acsomega.2c07393
ACS Omega 2023, 8, 10062−10076

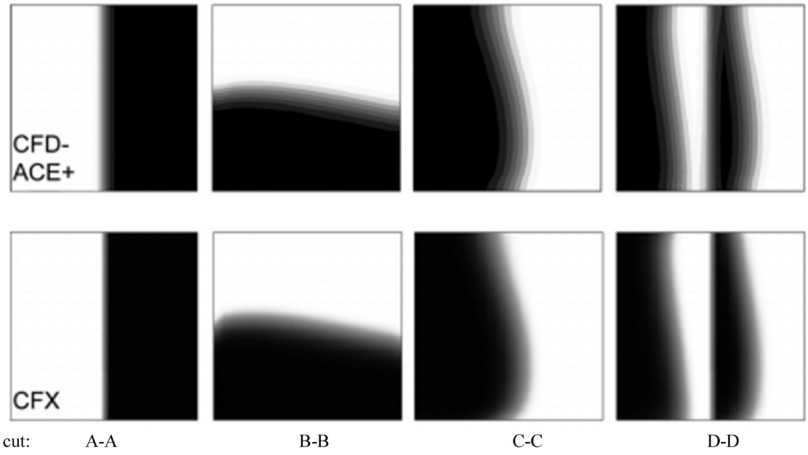


**Figure 2.** Lamination pattern after successive segments of the mixer unit from cut A−A to cut D−D (Experimental results of Glatzel et al.[25]).

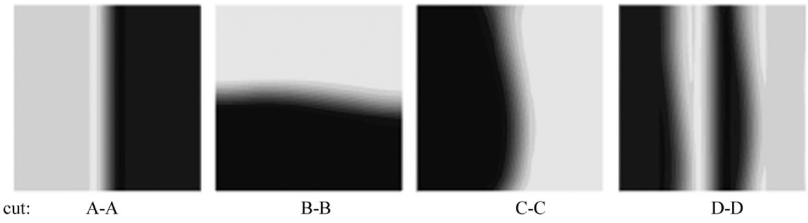


**Figure 3.** Lamination pattern after successive segments of the mixer unit from cut A−A to cut D−D (COMSOL numerical simulation results).

**Table 1. Comparison of Pressure Drop Data**

| method | resulting pressure drop in Pa |
|---|---|
| CFD-ACEX | 1.801 |
| CFX | 1.795 |
| COMSOL | 1.630 |

temperature $T_{ref}$ and model temperature $T$ are 343 K, the values of velocity field **u** and pressure $p$ in the initial value are both 0, the boundary condition of the wall is no-slip, the inlet injection velocity $U_0$ is 0.04 m·s$^{-1}$, and the outlet pressure $p_0$ is $1.4 \times 10^7$ Pa to ensure that the whole seepage process is in the miscible flooding state.

In the phase-field physical field, the interface thickness parameter and mobility adjustment parameter are default values. In the initial value, the model domain is filled with fluid 1 (oil), the contact angle of the wetted wall is 60°, and the injected fluid under the inlet phase-field condition is fluid 2 ($CO_2$). The surface tension coefficient $\sigma$ is $1 \times 10^{-9}$ N·m$^{-1}$ to eliminate the influence of surface tension on the calculation results.

In the physical field of transport of diluted species, the additional transfer mechanism is convection. The number of materials in the dependent variable is 1, the concentration is $c$, the model input temperature is 343 K, the diffusion coefficient $D$ of $CO_2$ is $1 \times 10^{-7}$ m$^2$·s$^{-1}$, the initial concentration $c$ in the model domain is 0 mol·m$^{-3}$, and the inlet concentration $c_0$ of substance $c$ ($CO_2$) is 10,404.55*step1($t$[1/s]) mol·m$^{-3}$, where step1($t$[1/s]) is a step function.

The solution is studied using transients, the physical field and variables are all selected, the time step is set to 0.0001 s, the separated solver is selected in the transient solver, the solver uses the PARDISO direct linear solver, the step size used in the solver is set to free, the maximum step size

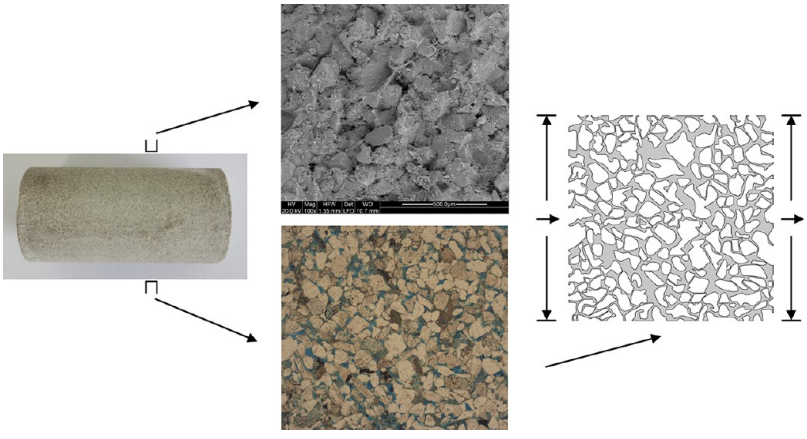

**Figure 4.** Two-dimensional model diagram.



https://doi.org/10.1021/acsomega.2c07393
ACS Omega 2023, 8, 10062−10076

Table 2. Physical Properties of $CO_2$ and Crude Oil at 343 K and 14 MPa[24]

| $CO_2$ density/kg·m$^{-3}$ | $CO_2$ viscosity/mPa·s | crude oil density/kg·m$^{-3}$ | crude oil viscosity/mPa·s | diffusion coefficient/m$^2$·s$^{-1}$ |
|---|---|---|---|---|
| 457.8 | 0.0342 | 705.1 | 0.57269 | $1 \times 10^{-7}$ |

constraint is set to automatic, and the solution method uses the backward difference formulation.

**2.6. Mesh Parameters.** The model size is 360 $\mu$m × 360 $\mu$m. The mesh shape is a free triangle, the number of elements is 94,521, the minimum element mass is 0.1559, the average element mass is 0.8024, the element area ratio is $1.713 \times 10^{-4}$, and the mesh area is 45,120 $\mu$m$^2$. The mesh division is shown in Figure 5

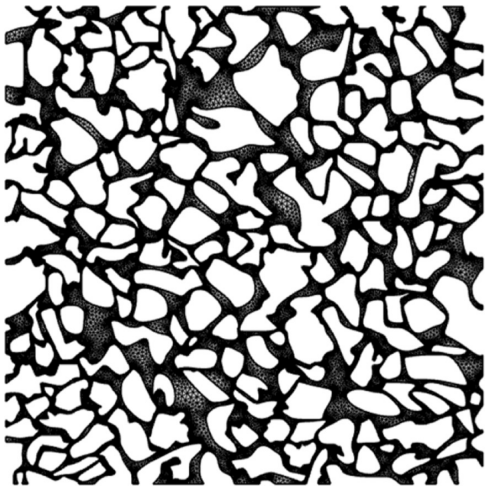

**Figure 5.** Mesh division of the two-dimensional model.

## 3. RESULTS AND DISCUSSION

**3.1. Microscopic Seepage Characteristics of $CO_2$ Miscible Flooding.** Figure 6 is the seepage process diagram of $CO_2$ miscible flooding, in which the color code from 0 to 1 represents the volume fraction of the oil phase. The figure shows that due to the difference in the distribution of the pore structure, the advancing speed of the leading edge of the mainstream line in the upper and lower parts of the model after $CO_2$ injection is greater than that in the middle, and when the lower mainstream line breaks through, the remaining oil is mainly concentrated in the upper and lower edges of the model and the middle part sandwiched by the two mainstream lines. With the increase in injection time, the remaining oil in the middle and edge is driven out, and at the end of the displacement, only part of the blind-end-shaped remaining oil and the droplet and column-shaped remaining oil controlled by the throat are left in the pore space. In the process of displacement, $CO_2$ is transferred and diffuses in the oil phase. The color of the contact part between crude oil and $CO_2$ changes from pure red to orange and yellow, and the color of the $CO_2$ front changes from pure blue to cyan and green. After multistage contact, a miscible area (the color is between pure blue and pure red) is formed. With increasing displacement time, the miscible area continues to expand. At the beginning of gas breakthrough, continuous gas injection will make the miscible area near the inlet continuously migrate to the middle and rear, $CO_2$ will continue to contact the remaining oil on both sides of the main flow line and advance toward the outlet, and the miscible area in the middle and near the outlet will continue to increase. As the injection time increases, the portion of gas seen at the outlet keeps increasing, the fluid in the miscible area keeps flowing out from the outlet, and the miscible area formed by $CO_2$ and crude oil reaches a maximum and then keeps decreasing. At the end of gas breakthrough, gas channeling will be formed, and $CO_2$ in the model will affect most of the pores. At this time, almost all of the miscible area will flow out of the outlet, and there is only a small amount of residual oil in the model.

Figure 7 shows the recovery efficiency curve with time. It can be seen from the figure that with the increase in $CO_2$ injection time, the oil recovery first rises rapidly and then gradually becomes flat. At the end of displacement, the oil recovery is 91.46%.

Figure 8 shows the change process of the $CO_2$ concentration in pores during miscible flooding. The color code in the figure represents the $CO_2$ concentration. The figure shows that after $CO_2$ injection, the concentration at the inlet is constant, convection−diffusion is fast at the upper and lower parts of the model, and the concentration in the front of the $CO_2$ miscible zone is lower than the internal concentration. With increasing injection time, the high concentration area gradually moves toward the middle of the model and the low concentration area at the outlet continuously increases. At the end of displacement, the area with high $CO_2$ concentration reaches the outlet, and only some areas with low concentration exist in the area where the remaining oil is concentrated.

Consider point M in the middle of the model and point N at the outlet to analyze the change in concentration with injection time. The positions of point M and point N are shown in Figure 9.

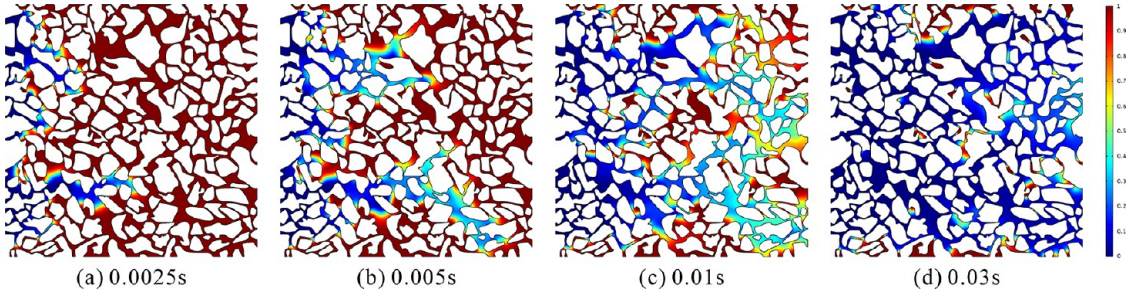


**Figure 6.** (a−d) Seepage process diagram of miscible $CO_2$ flooding.



https://doi.org/10.1021/acsomega.2c07393
ACS Omega 2023, 8, 10062−10076

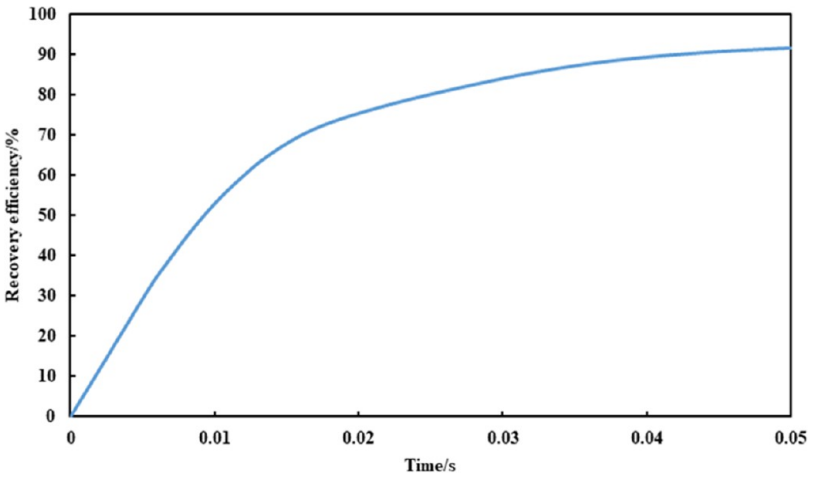


**Figure 7.** Recovery efficiency curve with time.

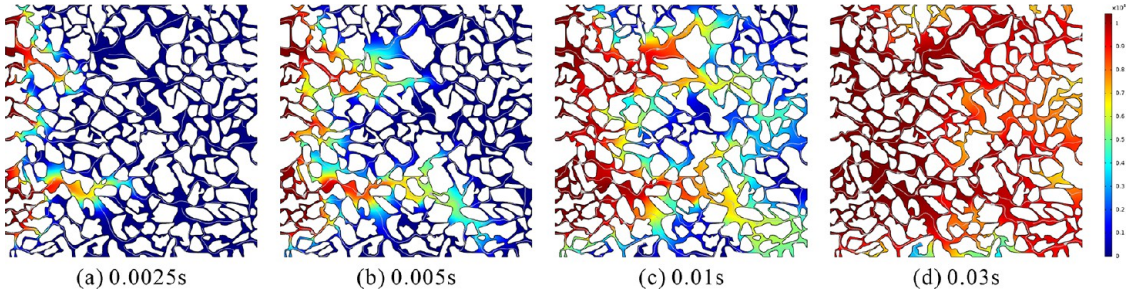


**Figure 8.** (a–d) Change in $CO_2$ concentration in pores during miscible flooding.

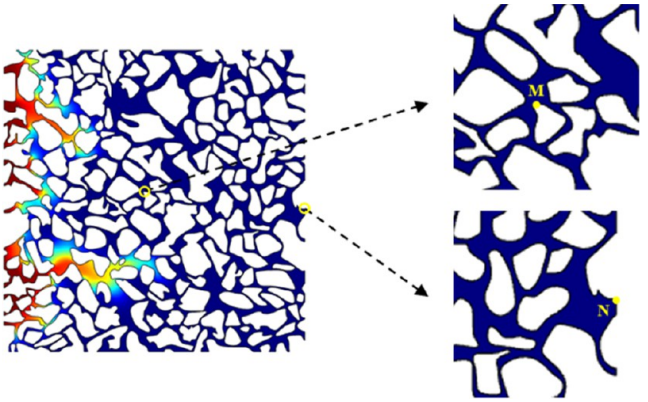


**Figure 9.** Location map of point M and point N.

The dimensionless $CO_2$ concentration is used to express the variation in $CO_2$ concentration at points M and N as follows

$$C_D = \frac{c}{c_0} \tag{23}$$

where $C_D$ is the dimensionless $CO_2$ concentration, dimensionless.

According to the research of Li et al.,[17] taking the dimensionless $CO_2$ concentration value as the judgment standard and taking Figure 10 as an example, the position when the dimensionless $CO_2$ concentration value reaches 0.95 is regarded as the $CO_2$ front, the position when the dimensionless $CO_2$ concentration value reaches 0.05 is regarded as the miscible zone front, and the middle area with the boundary of 0.05 and 0.95 is regarded as the miscible zone. When the $CO_2$ concentration at an outlet location is greater than 0, the dimensionless $CO_2$ concentration is also greater than 0, indicating that $CO_2$ has reached that outlet location. Gas breakthrough is defined as the displacement state when the dimensionless $CO_2$ concentration at a certain outlet is greater than 0. The injection time corresponding to the inflection point when the $C_D$ value is greater than 0 is regarded as the gas breakthrough time at this position. The injection time required when the miscible zone front at a certain point in the model gradually becomes the $CO_2$ front is regarded as the injection time used by the miscible zone to penetrate the position, also known as the penetration time. Gas channeling is an ineffective circulation phenomenon of gas after early gas discovery in production wells. It is defined in this paper that when the $CO_2$ front reaches the outlet N point, the miscible area completely passes through the outlet and the outlet position is completely gas channeling.

Table 3 shows that the penetration time required for the miscible area to penetrate point N is 0.03393 s, which is greater than that at the middle point M.

### 3.2. Influence of Different Factors on Microscopic Seepage Characteristics of $CO_2$ Miscible Flooding.

*3.2.1. Effect of Injection Velocity on Microscopic Seepage Characteristics of $CO_2$ Miscible Flooding.* To study the effect of injection velocity on the microscopic seepage characteristics of $CO_2$ miscible flooding, injection velocities of 0.01, 0.04, and 0.08 $m \cdot s^{-1}$ are selected for the displacement simulation.

Figure 11 shows the $CO_2$ miscible flooding seepage process at injection velocities of 0.01, 0.04, and 0.08 $m \cdot s^{-1}$. The figure shows that the greater the injection velocity is, the faster the $CO_2$ miscible displacement seepage at the same time and the larger the swept area. When the displacement time is less than



https://doi.org/10.1021/acsomega.2c07393
ACS Omega 2023, 8, 10062−10076

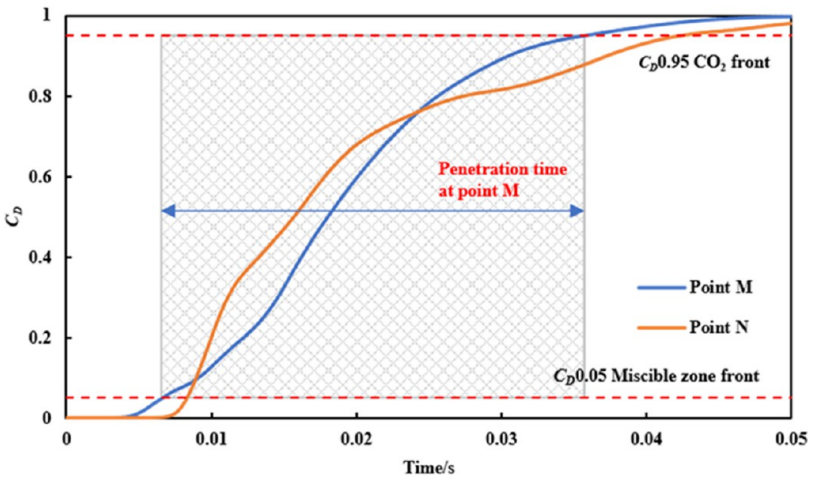


**Figure 10.** Schematic diagram of the penetration time in the $CO_2$ miscible area at different locations.

**Table 3. Migration Parameters in the Miscible Region Corresponding to Different Point Locations**

| point location | penetration time required for miscible area to penetrate the point/s | complete gas channeling time at N point/s |
|---|---|---|
| M | 0.02907 | |
| N | 0.03393 | 0.04227 |

0.005 s, the larger the injection velocity is, the larger the miscible area. The increase in injection velocity will advance the gas breakthrough time and accelerate the migration process of the miscible area to the outlet.

Figure 12 shows the change in oil recovery with time at different injection velocities. It can be seen from the figure that when the injection velocities are 0.04 and 0.08 m·s$^{-1}$, the recovery efficiency curve first rises rapidly and then tends to stabilize. When the injection velocity is 0.01 m·s$^{-1}$, the recovery efficiency curve increases during the displacement time and has not yet reached a stable state. Under the pore-scale simulation conditions, the maximum final recovery efficiency is 94.51% when the injection velocity is 0.08 m·s$^{-1}$, and the minimum final recovery efficiency is 61.28% when the injection velocity is 0.01 m·s$^{-1}$.

Figure 13 shows the variation in the $CO_2$ concentration in the pores during miscible flooding at different injection velocities. As seen from the figure, under the same injection concentration conditions, the larger the injection velocity is, the faster the $CO_2$ convection−diffusion, the larger the area of the high $CO_2$ concentration region, and the smaller the area of the upswept region under the same time.

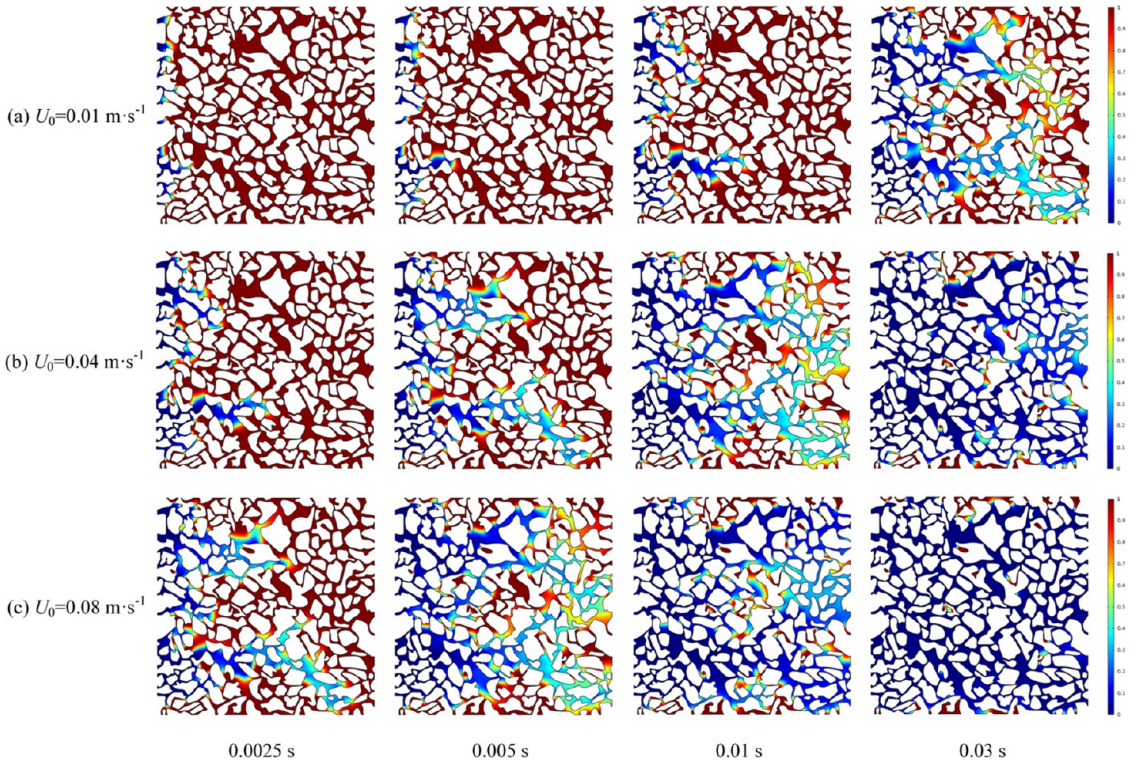


**Figure 11.** (a−c) Seepage process of $CO_2$ miscible flooding at different injection velocities.



https://doi.org/10.1021/acsomega.2c07393
ACS Omega 2023, 8, 10062−10076

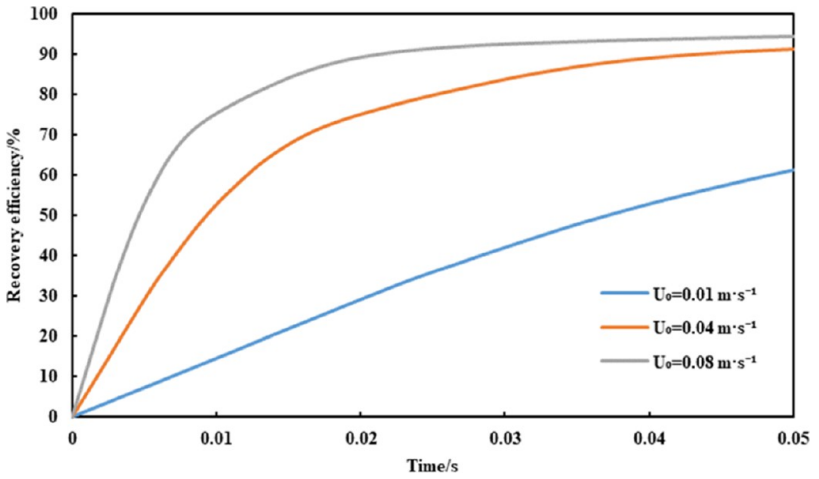


**Figure 12.** Variation in oil recovery with time at different injection velocities.

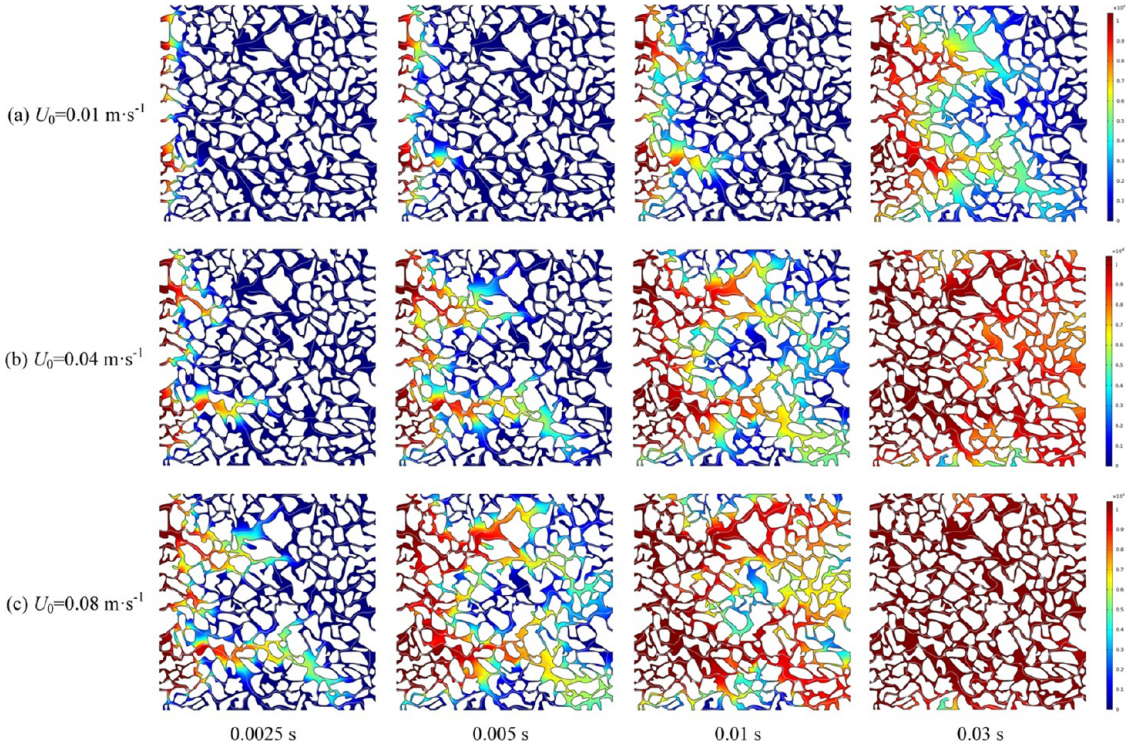


**Figure 13.** (a−c) Variation in $CO_2$ concentration in pores during miscible flooding at different injection velocities.

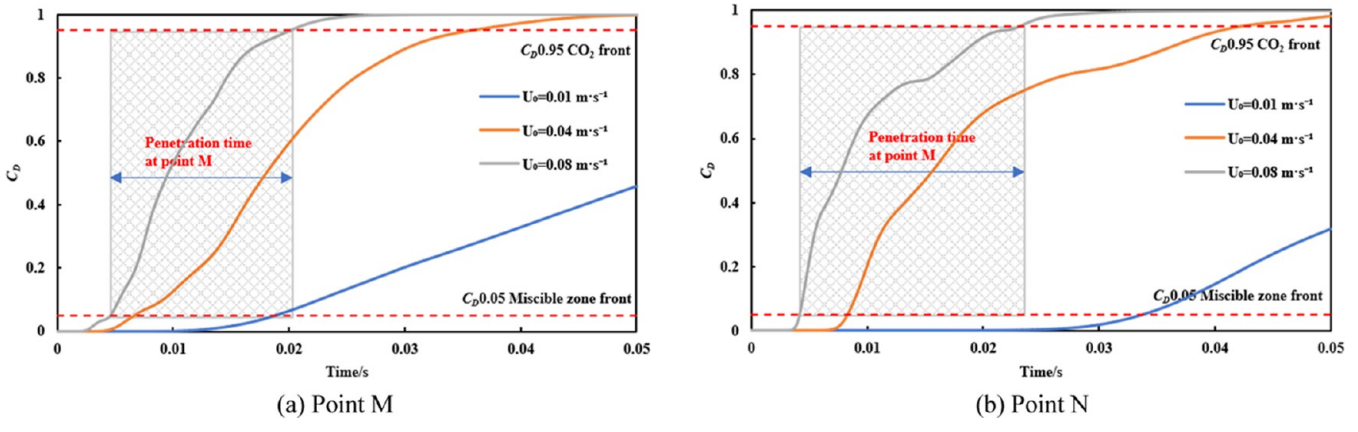


**Figure 14.** (a, b) Dimensionless $CO_2$ concentration variation curves of point M and point N at different injection velocities.



https://doi.org/10.1021/acsomega.2c07393
ACS Omega 2023, 8, 10062−10076

Figure 14 shows the dimensionless $CO_2$ concentration variation curves of point M and point N at different injection velocities. It can be seen from the figure that after gas is seen at each point, the dimensionless $CO_2$ concentration increases rapidly with time and then tends to be flat. When the injection velocity is 0.01 $m \cdot s^{-1}$, the dimensionless $CO_2$ concentration curve is still rising during the displacement time, and the final value of the dimensionless $CO_2$ concentration at point N is less than that at point M because of the late gas generation time. Table 4 shows that under the same injection conditions, the greater the injection speed is, the shorter the time for the miscible area to penetrate point M and point N, and the earlier the complete gas channeling time at point N.

**Table 4. Migration Parameters in the Miscible Region Corresponding to Different Point Locations**

| $U_0$ value/$m \cdot s^{-1}$ | point location | penetration time required for miscible area to penetrate the point/s | complete gas channeling time at N point/s |
|---|---|---|---|
| 0.01 | M | | |
| | N | | |
| 0.04 | M | 0.02907 | |
| | N | 0.03393 | 0.04227 |
| 0.08 | M | 0.01557 | |
| | N | 0.01901 | 0.02322 |

*3.2.2. Effect of Wettability on Microscopic Seepage Characteristics of $CO_2$ Miscible Flooding.* To study the effect of wall wettability on the microscopic seepage characteristics of $CO_2$ miscible flooding, contact angles of 60, 90, and 120° are selected for the displacement simulation.

Figure 15 shows the seepage process of $CO_2$ miscible flooding at different contact angles. It can be seen from the figure that the $CO_2$ swept area is close under different contact angles at the initial stage of displacement. With the increase in injection time, the increase in contact angle will weaken the interphase mass transfer between $CO_2$ and crude oil, the color of the remaining oil at the same location in the swept area will gradually deepen, and the volume fraction of the oil phase will increase. At the end of displacement, the larger the contact angle is, the more the remaining oil. When the contact angle gradually increases, the wall wettability gradually shifts from nonoil wet to oil wet, and the gas-phase seepage resistance gradually increases. The contact angle has little effect on the gas breakthrough time. When the gas breaks through the outlet, the smaller the contact angle is, the faster the miscible area increases.

Figure 16 shows the variation in oil recovery with time at different contact angles. It can be seen from the figure that at the initial stage of displacement, the oil recovery values under each contact angle are close. With increasing injection time, the larger the contact angle is, the smaller the increase in recovery and the smoother the curve. The final recovery efficiency is 91.46% when the contact angle is 60° and 85.46% when the contact angle is 120°.

Figure 17 shows the variation in the $CO_2$ concentration in the pores during miscible flooding at different contact angles. It can be seen from the figure that at the initial stage of $CO_2$ injection, the impact of the contact angle on the $CO_2$ concentration transfer process is not significant. With increasing injection time, the smaller the contact angle is, the higher the $CO_2$ concentration in the large pore, and the more $CO_2$ diffuses to the edge of the model. At the end of displacement, the $CO_2$ concentration at the remaining oil at the blind end of the model side part is lower at a contact angle of 120°, and the $CO_2$ concentration at the middle outlet of the model is higher.

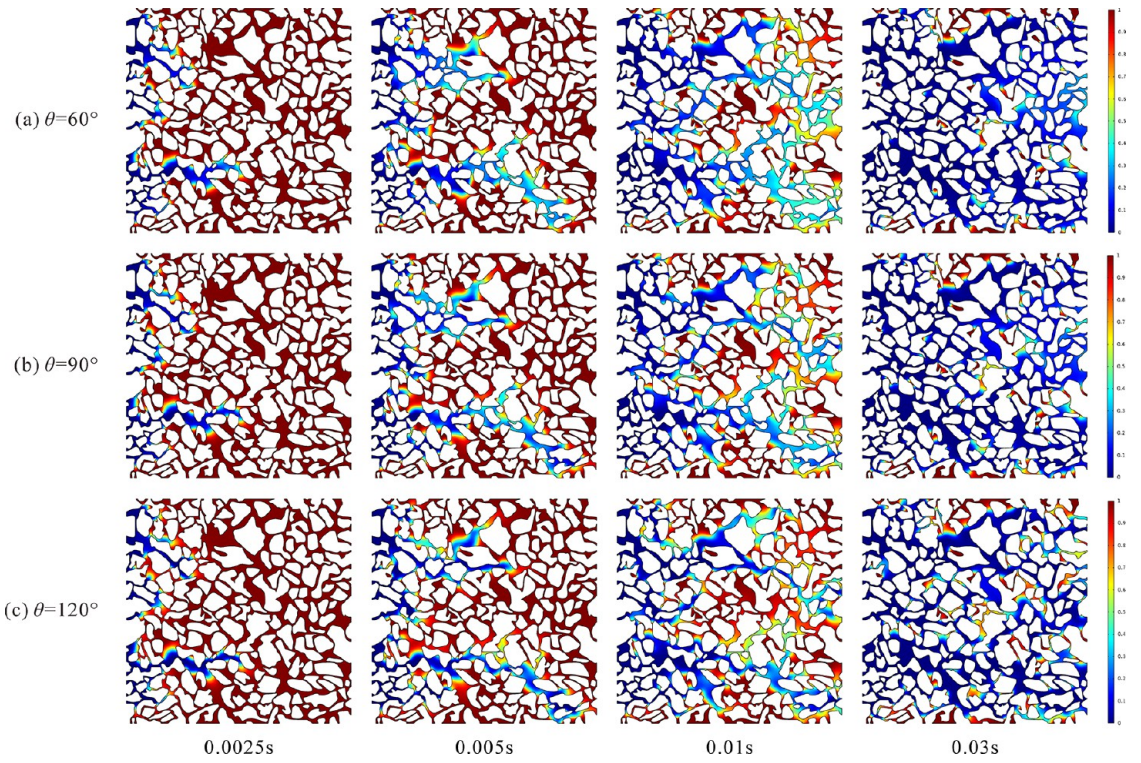


**Figure 15.** (a−c) Seepage process of $CO_2$ miscible flooding at different contact angles.



https://doi.org/10.1021/acsomega.2c07393
ACS Omega 2023, 8, 10062−10076

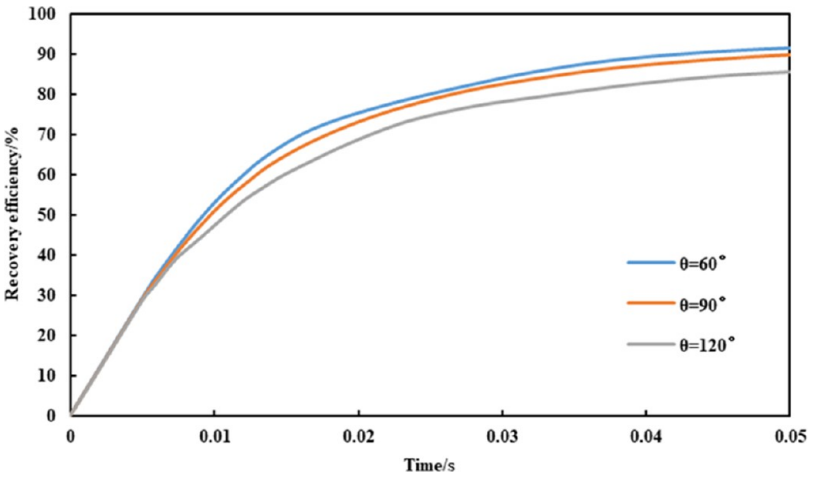


**Figure 16.** Variation in oil recovery with time at different contact angles.

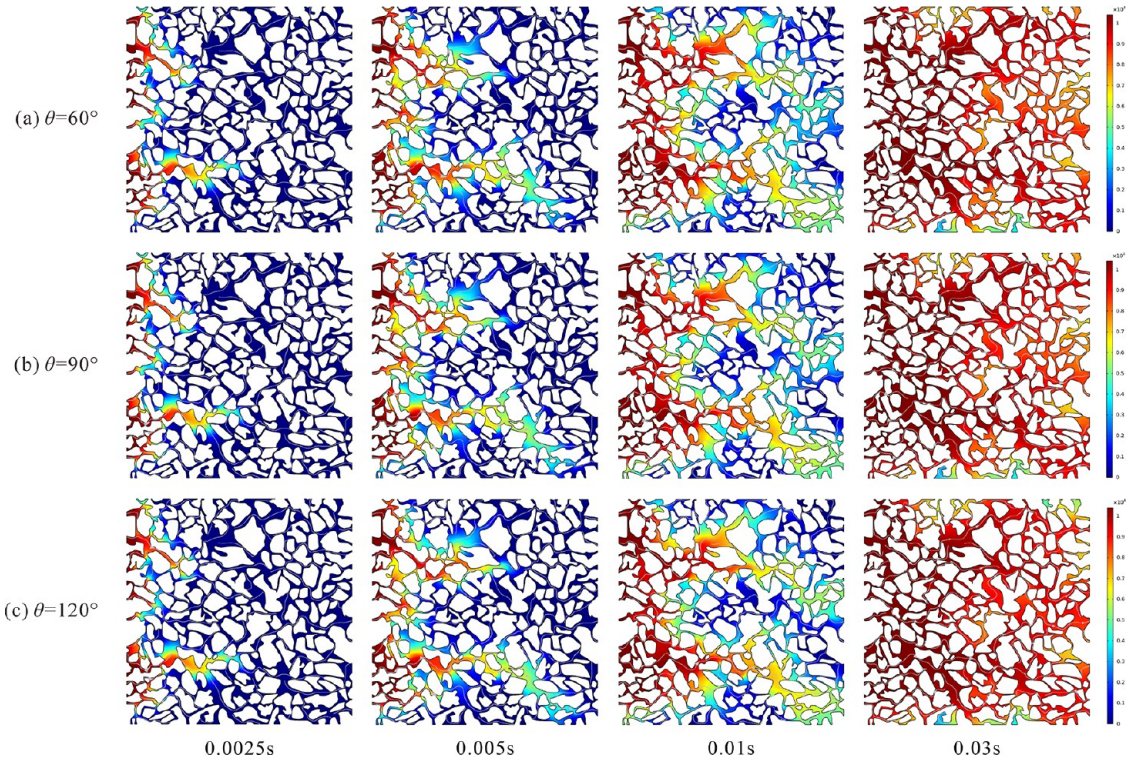


**Figure 17.** (a–c) Variation in $CO_2$ concentration in pores during miscible flooding at different contact angles.

Figure 18 shows the dimensionless $CO_2$ concentration variation curves of point M and point N at different contact angles. It can be seen from the figure that when the contact angle is 60 and 90°, the change trends of the dimensionless $CO_2$ concentration curves of point M and point N are close. When the contact angle is 120°, the curves of point M and point N change greatly before and in the middle of the penetration in the miscible region. At the end of the penetration in the miscible region, the curve change trend is gradually consistent with that when the contact angle is 60 and 90°. Table 5 shows that with increasing contact angle, the penetration time required for the miscible area to penetrate point M increases gradually. The penetration time at point N decreases first and then rises, and the complete gas channeling time gradually advances. At the same injection velocity, the advance of the gas channeling time will reduce the gas swept area, thereby reducing the recovery efficiency.

*3.2.3. Effect of the Diffusion Coefficient on the Microscopic Seepage Characteristics of $CO_2$ Miscible Flooding.* To study the effect of the diffusion coefficient on the microscopic seepage characteristics of $CO_2$ miscible flooding, diffusion coefficients of $1 \times 10^{-8}$, $5 \times 10^{-8}$, and $1 \times 10^{-7}$ $m^2 \cdot s^{-1}$ are selected for the displacement simulation.

Since the change in the diffusion coefficient in the physical field of transport of diluted species will not affect the speed and pressure of injected $CO_2$ in the laminar flow physical field, it will not affect the volume fraction of $CO_2$ and crude oil in the pores during miscible flooding. This section analyzes the concentration variations during $CO_2$ injection.

Figure 19 shows the variation in the $CO_2$ concentration in the pores during miscible flooding at different diffusion


https://doi.org/10.1021/acsomega.2c07393
ACS Omega 2023, 8, 10062−10076

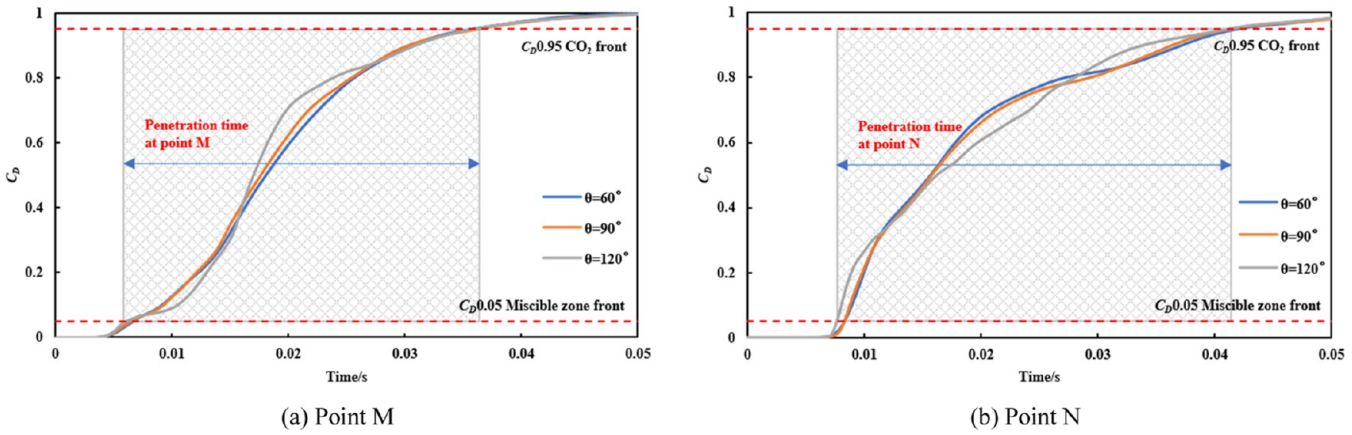


**Figure 18.** (a, b) Dimensionless $CO_2$ concentration variation curves of point M and point N at different contact angles.

**Table 5. Migration Parameters in the Miscible Region Corresponding to Different Point Locations**

| $\theta$ value/° | point location | penetration time required for miscible area to penetrate the point/s | complete gas channeling time at N point/s |
|---|---|---|---|
| 60 | M | 0.02907 | |
| | N | 0.03393 | 0.04227 |
| 90 | M | 0.02963 | |
| | N | 0.03326 | 0.04159 |
| 120 | M | 0.02983 | |
| | N | 0.03376 | 0.04145 |

coefficients. It can be seen from the figure that in the early and middle stages of injection, when the diffusion coefficient is low, $CO_2$ tends to convect and diffuse in the large pore space, resulting in a higher concentration in the large pore space. When the diffusion coefficient increases, the $CO_2$ concentration in the small pores and the parts that are hard to sweep at the edge of the model will gradually increase. After the gas breaks through the outlet, the increase in the diffusion coefficient is conducive to the diffusion and mass transfer of $CO_2$ in the remaining oil on both sides of the main flow line. At the end of displacement, the larger the diffusion coefficient is, the larger the $CO_2$ diffusion range is, and the smaller the low concentration area is.

Figure 20 shows the dimensionless $CO_2$ concentration variation curves of point M and point N at different diffusion coefficients. It can be seen from the figure that the larger the diffusion coefficient is, the earlier the miscible zone front and $CO_2$ front appear at each point. When $D = 1 \times 10^{-8}$ $m^2 \cdot s^{-1}$, the dimensionless $CO_2$ concentration curve at point M rises slowly in the early stage and faster in the middle stage; the dimensionless $CO_2$ concentration curve at point N rises faster in the early stage and slows down in the middle and late stages. Table 6 shows that the greater the diffusion coefficient is, the shorter the penetration time of the miscible area at each point

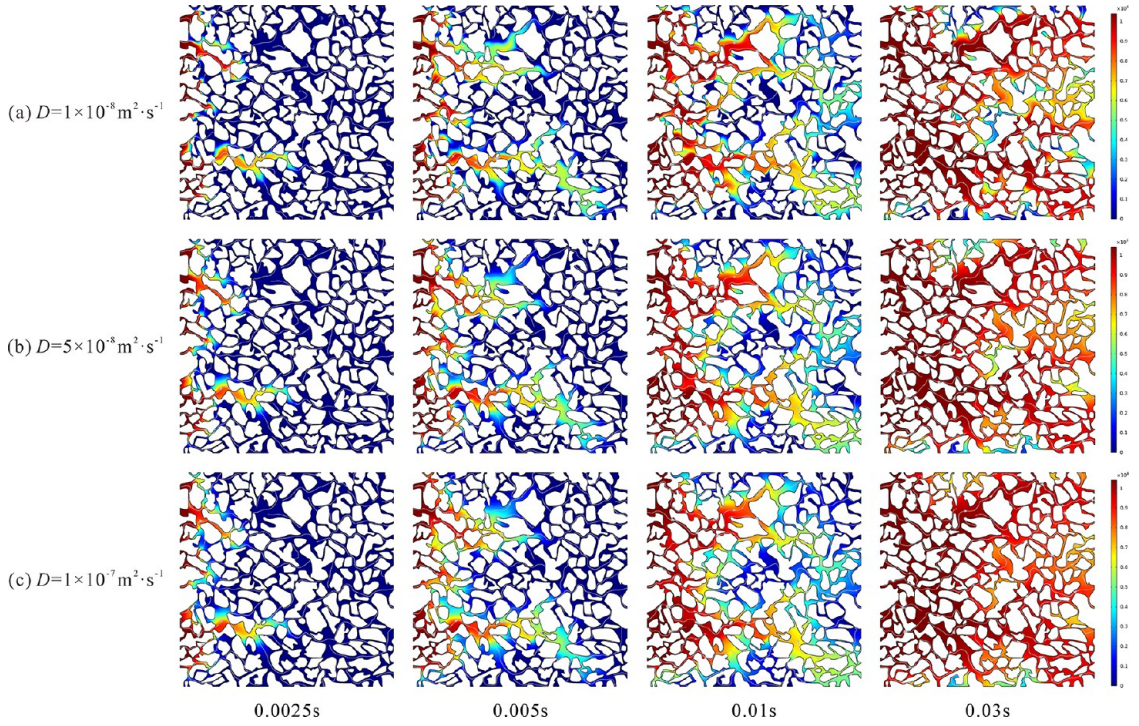


**Figure 19.** (a–c) Variation in $CO_2$ concentration in pores during miscible flooding at different diffusion coefficients.



https://doi.org/10.1021/acsomega.2c07393
ACS Omega 2023, 8, 10062−10076

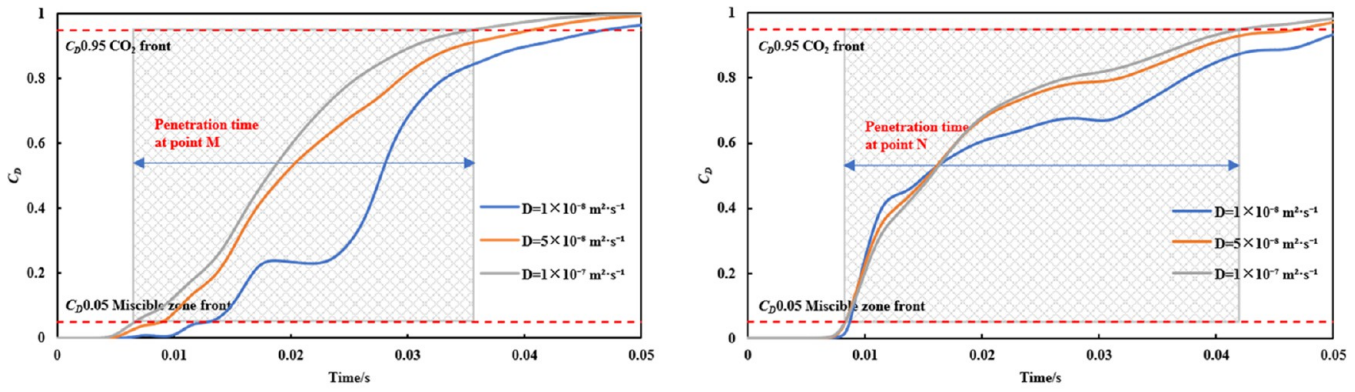


**Figure 20.** (a, b) Dimensionless $CO_2$ concentration variation curves of point M and point N at different diffusion coefficients.

**Table 6. Migration Parameters in the Miscible Region Corresponding to Different Point Locations**

| $D$ value/$m^2 \cdot s^{-1}$ | point location | penetration time required for miscible area to penetrate the point/s | complete gas channeling time at N point/s |
|---|---|---|---|
| $1 \times 10^{-8}$ | M | 0.03401 | |
| | N | | |
| $5 \times 10^{-8}$ | M | 0.03185 | |
| | N | 0.03842 | 0.04678 |
| $1 \times 10^{-7}$ | M | 0.02907 | |
| | N | 0.03393 | 0.04227 |

and the earlier the complete gas channeling time at point N. The increase in the diffusion coefficient accelerates the mass-transfer process of $CO_2$.

*3.2.4. Effect of Initial Injection Concentration on Microscopic Seepage Characteristics of $CO_2$ Miscible Flooding.* To study the effect of the initial injection concentration on the microscopic seepage characteristics of $CO_2$ miscible flooding, 10,404.55, 12,500, and 14772.73 mol·$m^{-3}$ are selected for displacement simulation.

Similar to the diffusion coefficient, the change in the initial injection concentration will not affect the speed and pressure of $CO_2$ injection, so it will not affect the volume fraction of $CO_2$ and crude oil in pores during miscible flooding. This section analyzes the concentration variations during $CO_2$ injection.

Figure 21 shows the variation in the $CO_2$ concentration in the pores during miscible flooding at different initial injection concentrations. As seen from the figure, the larger the initial injection concentration is, the larger the $CO_2$ concentration in the large pore and miscible regions in the swept area at the same time. When the gas breaks through the outlet, the $CO_2$ concentration in the same miscible region increases with

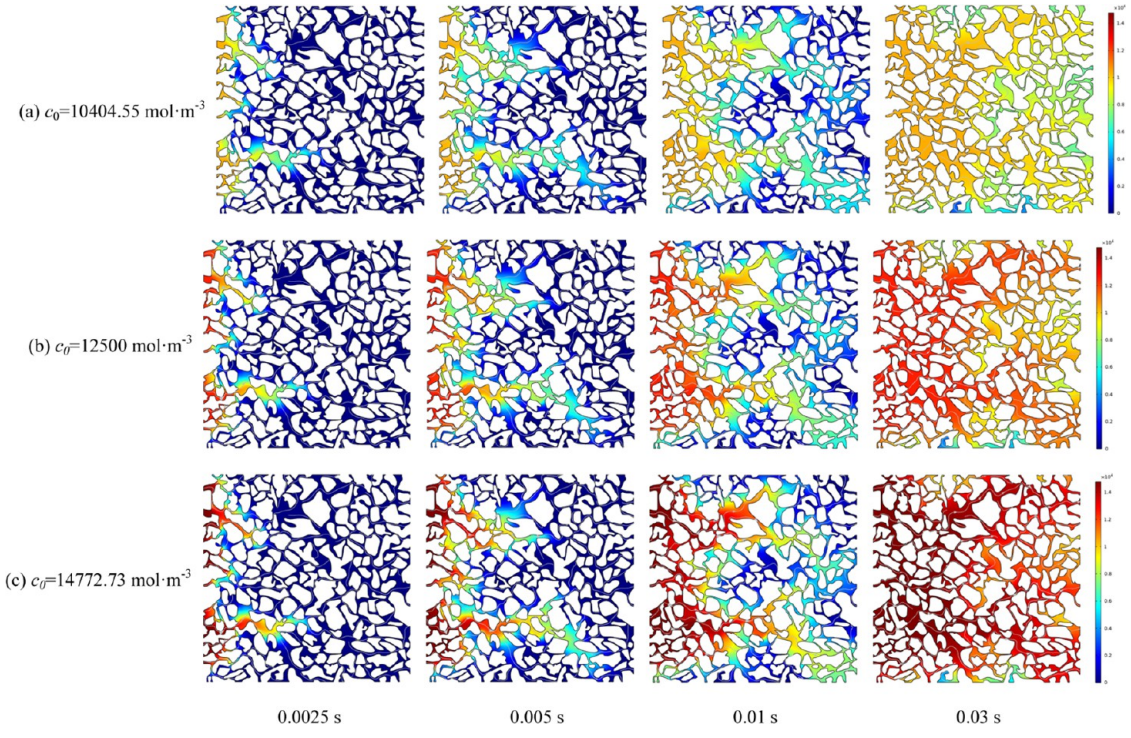


**Figure 21.** (a–c) Variation in $CO_2$ concentration in pores during miscible flooding at different initial injection concentrations.



https://doi.org/10.1021/acsomega.2c07393
ACS Omega 2023, 8, 10062−10076

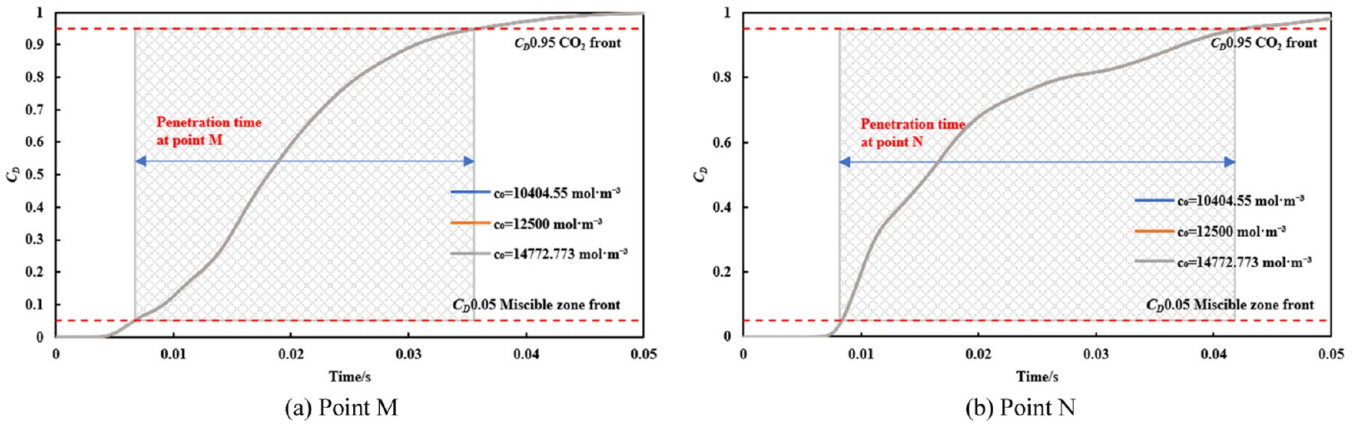


**Figure 22.** (a, b) Dimensionless $CO_2$ concentration variation curves of point M and point N at different initial injection concentrations.

increasing initial injection concentration. At the end of displacement, the $CO_2$ concentration at the blind end of the remaining oil at the edge of the model is low. The higher the initial injection concentration is, the greater the $CO_2$ concentration diffused in the remaining oil.

Figure 22 shows the dimensionless $CO_2$ concentration variation curves of point M and point N at different initial injection concentrations. As seen from the figure, the variation curves of the dimensionless $CO_2$ concentration at the two points do not differ with the change in the initial injection concentration. Table 7 shows that when the initial injection concentration changes, the penetration time of the miscible area at two points and the complete gas channeling time at point N are basically the same.

**Table 7. Migration Parameters in the Miscible Region Corresponding to Different Point Locations**

| $c_0$ value/mol·m$^{-3}$ | point location | penetration time required for miscible area to penetrate the point/s | complete gas channeling time at N point/s |
|---|---|---|---|
| 10404.55 | M | 0.02907 | |
| | N | 0.03393 | 0.04227 |
| 12500 | M | 0.02908 | |
| | N | 0.03393 | 0.04227 |
| 14772.73 | M | 0.02907 | |
| | N | 0.03393 | 0.04227 |

Figure 23 shows the actual $CO_2$ concentration variation curves of point M and point N at different initial injection concentrations. As seen from the figure, the rising trend of the curve increases and then slows down after seeing gas at each point, and the larger the initial injection concentration is, the larger the concentration value at the same injection time.

## 4. CONCLUSIONS

The following conclusions are summarized:

(1) After $CO_2$ injection, it preferentially diffuses to the large pores of the model and forms a miscible region with crude oil through interphase mass transfer, and the miscible region expands and is pushed toward the model outlet by the region of high $CO_2$ concentration as the displacement time increases. At the end of the replacement, only some blind-end remaining oil and throat-controlled droplets and column remaining oil remain in the pore space. The recovery efficiency curve rises rapidly and then gradually flattens out during miscible flooding.

(2) The increase in injection velocity will accelerate the seepage process of miscible $CO_2$ displacement. The larger the injection velocity is, the larger the area of the high $CO_2$ concentration region at the same time, and the less remaining oil is not displaced. The increase in injection velocity will shorten the time for the miscible area to penetrate point M and point N and advance the time for complete gas channeling at point N.

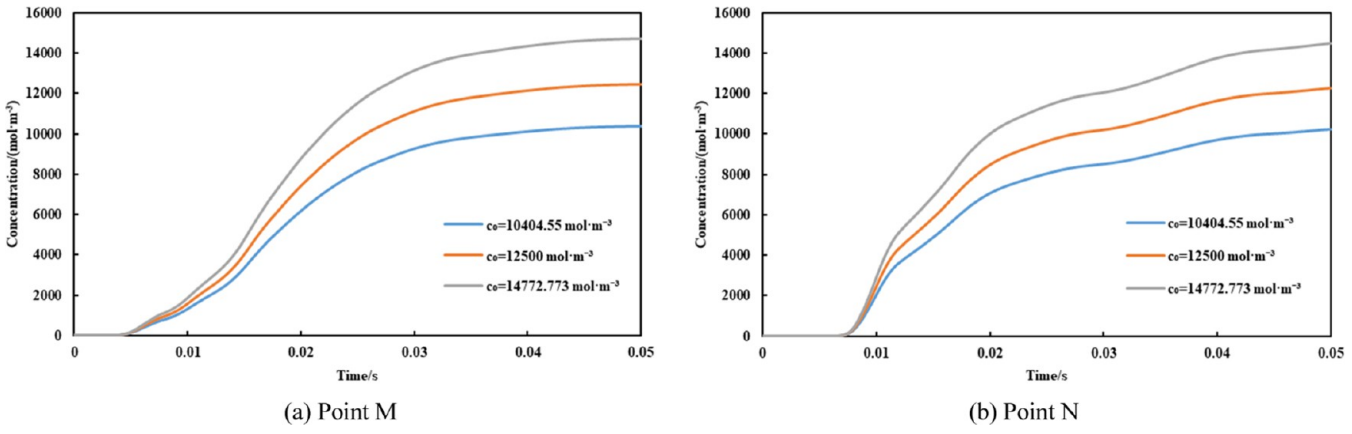


**Figure 23.** (a, b) Actual $CO_2$ concentration variation curves of point M and point N at different initial injection concentrations.



https://doi.org/10.1021/acsomega.2c07393
ACS Omega 2023, 8, 10062−10076

(3) The increase in contact angle will weaken the interphase mass transfer between $CO_2$ and crude oil. With increasing injection time, the smaller the contact angle is, the higher the $CO_2$ concentration in the large pores, and the more $CO_2$ diffuses to the model edge. At the same injection velocity, the increase in contact angle will advance the time of complete gas channeling at point N and reduce the final recovery efficiency.

(4) When the diffusion coefficient increases, the $CO_2$ concentration in the small pores and the parts that are hard to reach at the model edge will gradually increase. At the end of the displacement, the larger the diffusion coefficient is, the larger the $CO_2$ diffusion range and the smaller the area of low concentration. The larger the diffusion coefficient is, the earlier the miscible zone front and $CO_2$ front of point M and point N appear, and the earlier the complete gas channeling time of point N.

(5) The higher the initial injection concentration is, the higher the $CO_2$ concentration in the large pores and miscible areas in the affected area at the same time. Under the same wetting conditions, when the injection velocity and diffusion coefficient are certain, the variation in the initial injection concentration has little effect on the variation curve of the dimensionless concentration with time at different locations.

## AUTHOR INFORMATION


### Corresponding Author

**Chuanzhi Cui** − *School of Petroleum Engineering, China University of Petroleum (East China), Qingdao, Shandong 266580, China;* orcid.org/0000-0002-8475-7013; Email: ccz2008@126.com

### Authors

**Jing Li** − *School of Petroleum Engineering, China University of Petroleum (East China), Qingdao, Shandong 266580, China;* orcid.org/0000-0003-1159-1320

**Zhongwei Wu** − *School of Petroleum Engineering, Yangtze University, Wuhan, Hubei 430199, China*

**Jiqing Yi** − *School of Petroleum Engineering, China University of Petroleum (East China), Qingdao, Shandong 266580, China*

**Ran Zong** − *School of Petroleum Engineering, China University of Petroleum (East China), Qingdao, Shandong 266580, China*

**Yihui Fu** − *School of Petroleum Engineering, China University of Petroleum (East China), Qingdao, Shandong 266580, China*

**Xingyuan Han** − *School of Petroleum Engineering, China University of Petroleum (East China), Qingdao, Shandong 266580, China*

Complete contact information is available at: https://pubs.acs.org/10.1021/acsomega.2c07393


### Notes

The authors declare no competing financial interest.

## ACKNOWLEDGMENTS

This work was financially supported by the National Natural Science Foundation of China (No. 51974343) and the Postdoctoral Science Foundation of China (No. 2021M703588).

## ABBREVIATIONS

$\mathbf{u}$ =fluid velocity, $m \cdot s^{-1}$
$\rho$ =fluid density, $kg \cdot m^{-3}$
$t$ =time, s; $p$ is the pressure, Pa
$\mathbf{I}$ =identity matrix
$\mu$ =fluid viscosity, Pa·s
$\mathbf{F}_{st}$ =surface tension force between two phases, $Pa \cdot m^{-1}$
$U_0$ =normal inflow velocity, $m \cdot s^{-1}$
$\mathbf{n}$ =normal vector
$\hat{p}_0$ =outlet pressure, P
$\phi$ =phase-field variable, dimensionless
$\gamma$ =mobility, $m^3 \cdot s \cdot kg^{-1}$
$\lambda$ =mixing energy density, N
$\varepsilon$ =interface thickness parameter, m
$\psi$ =phase-field help variable
$\chi$ =mobility adjustment parameter, $m \cdot s \cdot kg^{-1}$
$\sigma$ =surface tension coefficient, $N \cdot m^{-1}$
$G$ =chemical potential, $J \cdot m^{-3}$
$V_{f,1}$ =volume fraction of oil phase, dimensionless
$V_{f,2}$ =volume fraction of $CO_2$, dimensionless
$\theta$ =contact angle, °
$V_f$ =fluid volume fraction, dimensionless
$D$ =diffusion coefficient, $m^2 \cdot s^{-1}$
$c$ =$CO_2$ concentration in the pore space, $mol \cdot m^{-3}$
$c_0$ =$CO_2$ injection concentration at the inlet, $mol \cdot m^{-3}$

## REFERENCES


(1) Zhu, G.; Yao, J.; Li, A.; Sun, H.; Zhang, L. Pore-scale investigation of carbon dioxide-enhanced oil recovery. *Energy Fuels* **2017**, *31*, 5324−5332.

(2) Fan, L.; Chen, J.; Zhu, J.; Nie, X.; Li, B.; Shi, Z. Experimental Study on Enhanced Shale Oil Recovery and Remaining Oil Distribution by $CO_2$ Flooding with Nuclear Magnetic Resonance Technology. *Energy Fuels* **2022**, *36*, 1973−1985.

(3) Xu, B. $CO_2$ miscible flooding in low permeability sandstone reservoirs and its influence on crude oil properties. *Pet. Sci. Technol.* **2017**, *35*, 2024−2029.

(4) Shaver, R. D.; Robinson, R. L., Jr; Gasem, K. A. M. An automated apparatus for equilibrium phase compositions, densities, and interfacial tensions: data for carbon dioxide + decane. *Fluid Phase Equilib.* **2001**, *179*, 43−66.

(5) Mohammadmoradi, P.; Taheri, S.; Bryant, S. L.; Kantzas, A. Solvent diffusion and dispersion in partially saturated porous media: An experimental and numerical pore-level study. *Chem. Eng. Sci.* **2018**, *191*, 300−317.

(6) Yang, W.; Zhang, L.; Liu, Y.; Zhao, Y.; Jiang, L.; Yang, M.; Wang, Z.; Wang, D.; Song, Y. Dynamic stability characteristics of fluid flow in $CO_2$ miscible displacements in porous media. *RSC Adv.* **2015**, *5*, 34839−34853.

(7) Zhao, Y.; Zhang, Y.; Lei, X.; Zhang, Y.; Song, Y. $CO_2$ flooding enhanced oil recovery evaluated using magnetic resonance imaging technique. *Energy* **2020**, *203*, No. 117878.

(8) Song, Y.; Yang, W.; Wang, D.; Yang, M.; Jiang, L.; Liu, Y.; Zhao, Y.; Dou, B.; Wang, Z. Magnetic resonance imaging analysis on the in-situ mixing zone of $CO_2$ miscible displacement flows in porous media. *J. Appl. Phys.* **2014**, *115*, No. 244904.

(9) Xiaolong, C.; Yiqiang, L.; Xiang, T.; Huan, Q.; Xuebing, S.; Jian, L. Effect of gravity segregation on $CO_2$ flooding under various pressure conditions: Application to $CO_2$ sequestration and oil production. *Energy* **2021**, *226*, No. 120294.

(10) Hoteit, H. Modeling diffusion and gas−oil mass transfer in fractured reservoirs. *J. Pet. Sci. Eng.* **2013**, *105*, 1−17.

(11) Hao, Y.; Li, J.; Kong, C.; Guo, Y.; Lv, G.; Chen, Z.; Wei, X. Migration behavior of $CO_2$-crude oil miscible zone. *Pet. Sci. Technol.* **2021**, *39*, 959−971.

(12) Kwon, S.; Lee, W. Parameter estimation in multiple contact $CO_2$ miscibility simulation with uncertain experimental core flooding data. *Korean J. Chem. Eng.* **2012**, *29*, 750−755.
(13) Ma, D. S.; Zhang, K.; Qin, J. S. Flow properties of $CO_2$/crude oil in miscible phase flooding. *Pet. Sci. Technol.* **2010**, *28*, 1427−1433.
(14) Li, W.; Yu, H.; Yang, Z.; Li, J.; Chen, X.; Ma, L. Experimental study on the sweep law of $CO_2$ miscible flooding in heterogeneous reservoir in Jilin. *Energies* **2022**, *15*, 5755.
(15) Yang, W.; Song, Y.; Liu, Y.; Zhao, Y.; Zhu, N.; Jiang, L. $CO_2$ Miscible Simulation for Magnetic Resonance Imaging Coreflood Tests. *Energy Procedia* **2013**, *37*, 6936−6941.
(16) Cai, M.; Su, Y.; Hao, Y.; Guo, Y.; Elsworth, D.; Li, L.; Li, D.; Li, X. Monitoring oil displacement and $CO_2$ trapping in low-permeability media using NMR: A comparison of miscible and immiscible flooding. *Fuel* **2021**, *305*, No. 121606.
(17) Li, J.; Cui, C.; Wu, Z.; Wang, Z.; Wang, Z.; Yang, H. Study on the migration law of $CO_2$ miscible flooding front and the quantitative identification and characterization of gas channeling. *J. Pet. Sci. Eng.* **2022**, *218*, No. 110970.
(18) Chen, M.; Cheng, L.; Cao, R.; Lyu, C.; Wang, D.; Wang, S.; Rao, X. Carbon dioxide transport in radial miscible flooding in consideration of rate-controlled adsorption. *Arabian J. Geosci.* **2020**, *13*, No. 38.
(19) Garmeh, G.; Johns, R. T.; Lake, L. W. Pore-scale simulation of dispersion in porous media. *Spe Journal* **2009**, *14*, 559−567.
(20) Khan, M.; Raza, A.; Zahoor, M. K.; Gholami, R. Feasibility of miscible $CO_2$ flooding in hydrocarbon reservoirs with different crude oil compositions. *J. Pet. Explor. Prod. Technol.* **2020**, *10*, 2575−2585.
(21) Ju, B.; Wu, Y. S.; Qin, J.; Fan, T.; Li, Z. Modeling $CO_2$ miscible flooding for enhanced oil recovery. *Pet. Sci.* **2012**, *9*, 192−198.
(22) Afshari, S.; Hejazi, S. H.; Kantzas, A. Role of medium heterogeneity and viscosity contrast in miscible flow regimes and mixing zone growth: A computational pore-scale approach. *Phys. Rev. Fluids* **2018**, *3*, No. 054501.
(23) Bhatti, A. A.; Raza, A.; Mahmood, S. M.; Gholami, R. Assessing the application of miscible $CO_2$ flooding in oil reservoirs: a case study from Pakistan. *J. Pet. Explor. Prod. Technol.* **2019**, *9*, 685−701.
(24) Ma, Q.; Zheng, Z.; Fan, J.; Jia, J.; Bi, J.; Hu, P.; Wang, Q.; Li, M.; Wei, W.; Wang, D. Pore-scale simulations of $CO_2$/oil flow behavior in heterogeneous porous media under various conditions. *Energies* **2021**, *14*, 533.
(25) Glatzel, T.; Litterst, C.; Cupelli, C.; Lindemann, T.; Moosmann, C.; Niekrawietz, R.; Streule, W.; Zengerle, R.; Koltay, P. Computational fluid dynamics (CFD) software tools for microfluidic applications−A case study. *Comput. Fluids* **2008**, *37*, 218−235.


https://doi.org/10.1021/acsomega.2c07393
*ACS Omega* 2023, 8, 10062−10076